



# A Functionally Graded Cathode Architecture for Extending the Cycle-Life of Potassium-Oxygen Batteries

Paul Gilmore<sup>[a]</sup> and Vishnu B. Sundaresan\*<sup>[a]</sup>

Potassium-Oxygen ( $K-O_2$ ) batteries have a high theoretical energy density of  $935 \text{ Wh kg}^{-1}$  due to a single-electron redox process in the reversible formation of potassium superoxide. Despite this advantage, standard  $K-O_2$  batteries have limited cycle-life (5–10) due to molecular oxygen crossover from cathode to anode, resulting in side reactions forming undesired superoxide on the anode. In this article, a  $K-O_2$  battery fabricated with a functionally-graded cathode (FGC) architecture is presented to address oxygen crossover at the cathode. This  $K-O_2$  battery lasts  $>125$  cycles with minimal loss in coulombic efficiency when charged/discharged to  $300 \mu\text{Ah}$  ( $238 \mu\text{Ah cm}^{-2}$ ). The FGC is comprised of a carbon fiber layer, microporous carbon and polypyrrole doped with hexafluorophosphate. It provides a scalable architecture for regulating  $K^+$

ion and oxygen transport at the cathode trilayer (liquid-solid-air) interface. The PPy( $\text{PF}_6^-$ ) formed on the cathode is observed to have an ORR rate two orders greater than that of carbon-based electrodes, as it promotes the reversible formation of potassium superoxide at the cathode, minimizes the transport of molecular oxygen into the electrolyte, and subsequently improves anode stability and cycle-life of the  $K-O_2$  battery. These improvements in performance with FGC come at a marginal increase in  $K-O_2$  battery material cost, which is estimated to be  $\$44 \text{ kWh}^{-1}$ . The combination of performance and cost  $\text{kWh}^{-1}$  makes this architecture the most cost-effective electrochemical energy storage device for stationary applications.

## 1. Introduction

Metal-air (or metal-oxygen batteries are some of the most energy dense electrochemical power sources.<sup>[1]</sup> For example, the theoretical energy density of a lithium-air battery is  $3623 \text{ Wh kg}^{-1}$ , and it is expected that a practical energy density of  $1700 \text{ Wh kg}^{-1}$  can be achieved on the cell level.<sup>[2]</sup> However, high overpotentials and side reactions during formation and decomposition of lithium peroxide result in capacity fade.<sup>[3]</sup> Potassium-oxygen ( $K-O_2$ ) batteries have a theoretical energy density of  $935 \text{ Wh kg}^{-1}$  and very low overpotential (50 mV) from a single step one-electron redox process to form stable potassium superoxide in the cathode.<sup>[4]</sup> Despite this advantage over  $\text{Li}-O_2$  batteries, standard  $K-O_2$  batteries have poor cycle-life due to side reactions at the anode that lead to instability. The simplest  $K-O_2$  battery is constructed from porous carbon cathode (air side), dimethoxyethane (DME) containing  $\text{KPF}_6$  electrolyte and metallic potassium anode. Combined experimental studies and DFT calculations show that side reactions at the anode are likely driven by the interaction of potassium with DME solvent and the molecular oxygen crossing over from the cathode.<sup>[5]</sup> The products formed from these side reactions ( $\text{KO}_2$ ,  $\text{KOH}$ ,  $\text{K}_2\text{CO}_3$ ,  $\text{KCOOH}$ ) lead to passivation of the anode and limit the battery life to less than 5–10 cycles.<sup>[4,6, 7]</sup> Therefore, preventing the side reactions between the potassium metal

anode, crossover oxygen and ether solvent holds the key towards developing a long cycle-life potassium-air battery. Wu and coworkers have demonstrated anode protection by forming a selectively permeable solid electrolyte interphase (SEI) on the anode. The surface of K metal is modified by adding a  $\text{K}^+$  salt that forms an ether and  $O_2$  impermeable SEI. In one such approach, KTFSI is added to the electrolyte so that the TFSI anion forms a stable SEI on K metal and protects the anode surface.<sup>[6]</sup> The  $K-O_2$  battery with KTFSI salt in DME was stable for more than 700 hours, although the low ionic conductivity of the SEI increased the overpotential by 350 mV. Despite the long cycle-life, a high overpotential will lead to an overall decrease in energy density and specific power, thereby negating the advantages of  $\text{KO}_2$  battery chemistry. In a second approach, potassium metal was treated with KFSI to form an SEI from K metal and FSI anion before assembling it into a  $K-O_2$  battery. The  $K-O_2$  battery was constructed with this KFSI treated K metal, KTFSI salt in DME and carbon cathode. This SEI was shown to promote efficient plating and stripping of potassium on the anode, minimized the formation of dendrites and thereby leading to a cycle-life of  $\sim 800$  hours and 200 cycles (for a charging/discharging current of  $50 \mu\text{A cm}^{-2}$  with a 2 hour charging/discharging period for a capacity of  $100 \mu\text{Ah}$ ).<sup>[8]</sup>

In order to evaluate the advantages of these anode protection strategies against the cost of required materials, a comparative cost analysis is performed and details of this analysis with a spreadsheet is provided in SI. The results shown in Figure 1 are calculated using established cost structure for Li-air batteries and indicate a twenty-fold increase at a scale of manufacture comparable to Li-ion batteries. The base cost of  $K-O_2$  battery with K metal/membrane separator/carbon fiber

[a] P. Gilmore, Prof. V. B. Sundaresan  
Department of Mechanical and Aerospace Engineering  
The Ohio State University  
201 W 19th Avenue, Columbus, OH – 43210, USA  
E-mail: sundaresan.19@osu.edu

 Supporting information for this article is available on the WWW under <https://doi.org/10.1002/batt.201900025>

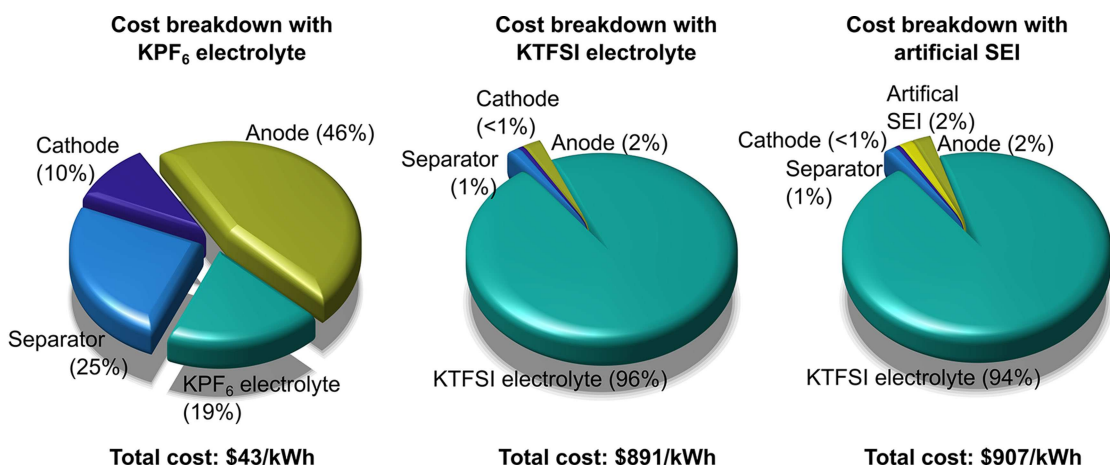


**Figure 1.** Cost breakdown of K–O<sub>2</sub> battery materials at the cell level for different electrolyte formulations: K–O<sub>2</sub> battery with KPF<sub>6</sub> electrolyte (left), K–O<sub>2</sub> battery with KTFSI electrolyte (middle), and K–O<sub>2</sub> battery with artificial anode SEI pre-formed with KFSI electrolyte (right).

paper is estimated to be about \$43 kWh<sup>-1</sup>. A pre-treatment of K metal with KFSI to form the SEI adds about \$15.6 kWh<sup>-1</sup> and KTFSI electrolyte adds ~\$850 kWh<sup>-1</sup>. The contemporary approaches to prolong the cycle-life of K–O<sub>2</sub> battery require expensive ionic liquids (KTFSI), and cost could potentially become an obstacle for large-scale deployment. From this analysis, it is clear that the total materials cost for a K–O<sub>2</sub> battery with long cycle-life should be as competitive as the best lithium-ion batteries (\$100–\$150 kWh<sup>-1</sup>).<sup>[9]</sup> Hence, it is anticipated that the economically feasible battery chemistry for K–O<sub>2</sub> battery should not use ionic liquids and consider design alternatives with KPF<sub>6</sub> salt in the electrolyte. With these constraints and towards the goal of a long cycle-life K–O<sub>2</sub> battery, this article presents an alternative strategy of using a membrane barrier in the cathode that supports oxygen reduction reaction/oxygen evolution reaction (ORR/OER), allow bidirectional K<sup>+</sup> ion transport and minimize the transport of oxygen to the electrolyte.

## 2. Functionally Graded Cathode

The functional objective of this cathode is to minimize the presence of extraneous molecular oxygen at the electrolyte-air interface in the cathode, therefore preventing oxygen diffusion to the anode. Towards this objective, a cathode design that has high porosity near the air side for accumulation of discharge products and facile oxygen diffusion, and low porosity and high catalytic activity on the separator side (inner layer) to limit molecular oxygen concentration is presented in this article. In addition, a polypyrrole layer is added to the electrolyte side to enhance the ORR/OER reactions in the cathode and maximize the utilization of cathode. Due to the gradually varying porosity and electrochemical function of this cathode, this design is referred to as a functionally-graded cathode (FGC).

It should be noted that functionally graded electrodes have been studied for lithium air batteries and fuel cells (PEMFC, SOFC and MeOH FC).<sup>[10,11]</sup> In lithium-air batteries, the varying

pore size through the thickness of the cathode has been shown to enhance the utilization of cathode.<sup>[12]</sup> The FGC offers a large surface area to volume ratio and increases the accessibility of catalytic surfaces in fuel cells. It should be noted that such (FGC) designs for K–O<sub>2</sub> batteries do not exist and this article presents the first demonstration of integrating an electroactive material in the cathode that enhances OER/ORR in K–O<sub>2</sub> batteries. Each of these functionally-graded cathodes has different design objectives, and the FGC presented here is translatable to Li–O<sub>2</sub> batteries to reduce O<sub>2</sub> crossover to lithium anodes. In addition, the FGC structure does not sacrifice on rate performance compared to uniform porous cathodes. The majority of the cathode thickness (74%) consists of porous carbon fiber, enabling fast oxygen diffusion to active sites. The oxygen-constricting PPy(PF<sub>6</sub>) layer increases the resistance for oxygen flux to the separator, resulting in a larger buildup of O<sub>2</sub> in the cathode.

### 2.1. Design Considerations

A solid model drawn to scale for this K–O<sub>2</sub> battery is shown in Figure 2 and the inset shows the layered arrangement of the FGC. The theoretical basis for oxygen transport across the FGC in K–O<sub>2</sub> battery is presented from 1-D mass transport equation:

$$\varepsilon \frac{\partial C_{O_2}}{\partial t} = \nabla \cdot (D_{eff} \nabla C_{O_2}) - \frac{R_{O_2}}{F} \quad (1)$$

where  $C_{O_2}$  is the oxygen concentration in the liquid phase electrolyte,  $D_{eff}$  is the effective oxygen diffusion coefficient,  $\varepsilon$  is the porosity and  $R_{O_2}$  is the oxygen consumption rate per unit cathode volume.<sup>[13,14]</sup> The oxygen consumption rate can be modeled by the Tafel equation:<sup>[15]</sup>

$$R_{O_2} = \frac{i_o A_s C_{O_2}}{C_{O_2}^{ref}} \times e^{\left(\frac{RT}{4F}\right)} \quad (2)$$

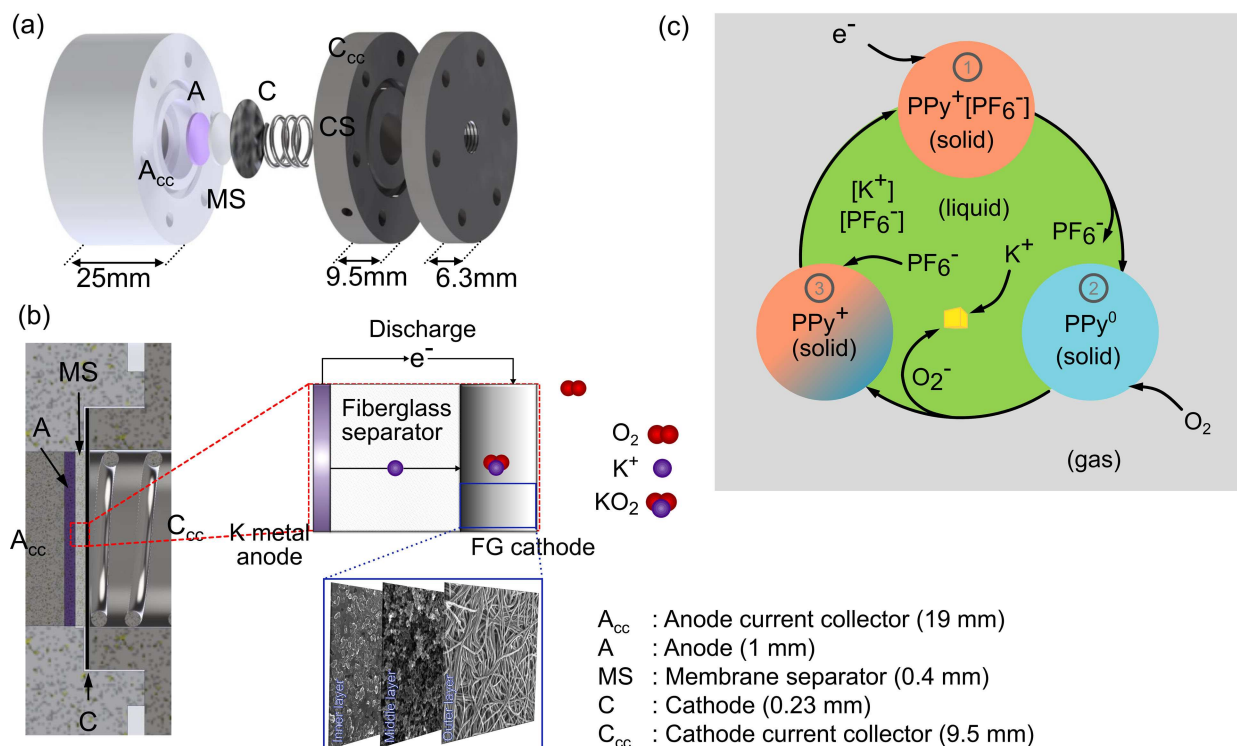


**Figure 2.** K–O<sub>2</sub> battery with functionally graded cathode (FGC) uses a layered architecture (a, b), the solid-liquid-air triple layer interface in the cathode is designed to have varying porosity, distribution of active material and ionic conductivity across the thickness so that the supply and demand of oxygen is regulated in the cathode. Electrochemical reaction steps of a single PPy redox site as it participates in oxygen reduction reaction is summarized in (c).

where  $i_o$  is the exchange current density for ORR on the cathode surface and  $A_s$  is the cathode specific surface area in  $\text{m}^2 \text{m}^{-3}$ . The oxygen flux across to the anode (oxygen crossover rate) is given by

$$J_{O_2}|_{x=0} = D_{eff}^s \frac{\partial C_{O_2}}{\partial x}|_{x=0} \quad (3)$$

where the anode surface is at  $x=0$ , and  $D_{eff}^s$  is the effective oxygen diffusion coefficient in the separator. From these equations, it is observed that  $J_{O_2}$  can be minimized while also maintaining high specific capacity by varying material properties and transport coefficients  $\varepsilon$ ,  $D_{eff}$  and  $i_o$  across the cathode thickness.

The variation in properties desired at the cathode is realized by a combination of carbon fiber paper, a microporous middle layer and a highly catalytic, dense inner layer (Figure 2(b)). In this article, polypyrrole is chosen for the inner layer due to its facile and scalable synthesis, electric conductivity, low gas permeability and support for ORR/OER.<sup>[16,17,18,19,20]</sup> It should be noted that PPy-based membranes have been applied in Li-air batteries by Cui et al to promote oxygen diffusion into the cathode on the air side using a tubular architecture.<sup>[21]</sup> PPy/carbon nanocomposite has been applied as a cathode in a hybrid Li-air battery, and it has been clearly demonstrated to support ORR with sufficiently high electrocatalytic activity.<sup>[22]</sup> Despite these initial reports on the use of PPy as a cathode

material in air batteries, this article will be first investigation to demonstrate the use of PPy and a FGC in K–O<sub>2</sub> battery.

## 2.2. Dopant Selection, Cathode Fabrication, and Characterization

Polypyrrole can be prepared with a wide selection of dopants. A bulky dopant in polypyrrole tends to lock itself in the polymer during electropolymerization, and PPy(DBS), PPy(DS), and PPy doped with various ionic liquid salts are good examples. From among these choices, PPy(DBS) has been studied extensively as actuators, sensors and in energy storage in polar solvents and some organic solvents. Towards the selection of dopant in PPy for the K–O<sub>2</sub> battery, cycling of PPy (DBS), PPy(PF<sub>6</sub>), PPy(TFSI), PPy(FC), PPy(Cl), PPy(PPS), PPy(DS) in DME + 0.5 M KPF<sub>6</sub> was performed via cyclic voltammetry. PPy (DBS), PPy(TFSI), PPy(Cl), PPy(PPS) experienced a considerable volumetric expansion and lost all electrochemical activity within a day. Polypyrrole doped with the other dopants either did not exhibit sufficient K<sup>+</sup> transport or electrochemical cycling in DME. The data from this experiment in Figure S2 demonstrates the incompatibility of PPy doped with a bulky anion (DBS<sup>-</sup>) with the ether solvent compared to PPy(PF<sub>6</sub>). Polypyrrole doped with PF<sub>6</sub><sup>-</sup> exhibited better stability in DME and produced stable cyclic voltammograms for extended periods of time. Hence, PF<sub>6</sub> was selected as the dopant and PPy

( $\text{PF}_6^-$ ) was used in the FGC of  $\text{K}-\text{O}_2$  battery presented in this article.

The substrate for preparing the FGC was chosen from commercially available gas diffusion electrode (Freudenberg H23C8). The H23C8 has a multi-layer architecture with a highly porous fibrous layer on one side and microporous layer on the other side as shown in Figure 3(a). During discharge, potassium superoxide will form in the pores of the cathode. It is important that the pores in the cathode at the cathode/separator interface are not completely blocked until the end of discharge so that  $\text{K}^+$  conduction can continue to exterior cathode sites for complete utilization of the internal volume. At the same time, smaller pore sizes are desirable to limit the local oxygen concentration since the flux across the cathode from the air side to the electrolyte side will depend on the cathode porosity. The FGC is designed to meet these conflicting demands by electropolymerizing PPy( $\text{PF}_6^-$ ) on the microporous carbon side of H23C8 substrate. From SEM, it is observed that the carbon fiber layer is approximately 170 microns thick and the pore size is large ( $>50 \mu\text{m}$ ). The microporous region is about 50 microns thick and has pore sizes ranging from 200–500 nm. PPy( $\text{PF}_6^-$ ) forms a very thin layer on the top surface of the microporous layer and the thickness and porosity of this

layer depends on the electropolymerized charge. PPy spans across an entire pore at a sufficiently high charge density depending on the substrate pore size, electrolyte concentration and morphology.<sup>[23,24,20]</sup> Therefore, precise control of the porosity is essential for the successful application of the functionally graded cathode and the areal charge density of PPy( $\text{PF}_6^-$ ) was varied between  $100 \text{ mC cm}^{-2}$  and  $300 \text{ mC cm}^{-2}$  to investigate the effect of porosity on battery performance.

Porosity of the FGC was characterized by measuring the Gurley value for oxygen permeability using the experimental setup shown in Figure 3(b) and described in SI. The measured Gurley value of the fibrous layer is almost zero and no pressure drop was registered in the characterization setup. The Gurley value for the fibrous carbon layer and microporous carbon layer was measured to be 76 seconds (Figure 3b). This value is lower than the specification given for air permeability on the manufacturer spec sheet (90 s). The steady state pressure drop was a measured variable and not a control input, and the permeability was normalized to the standard Gurley pressure drop of 0.176 psi. This may explain the deviation if the permeability is pressure dependent. The microporous layer therefore provides most of the resistance to oxygen diffusion through the cathode. Oxygen permeability further decreases

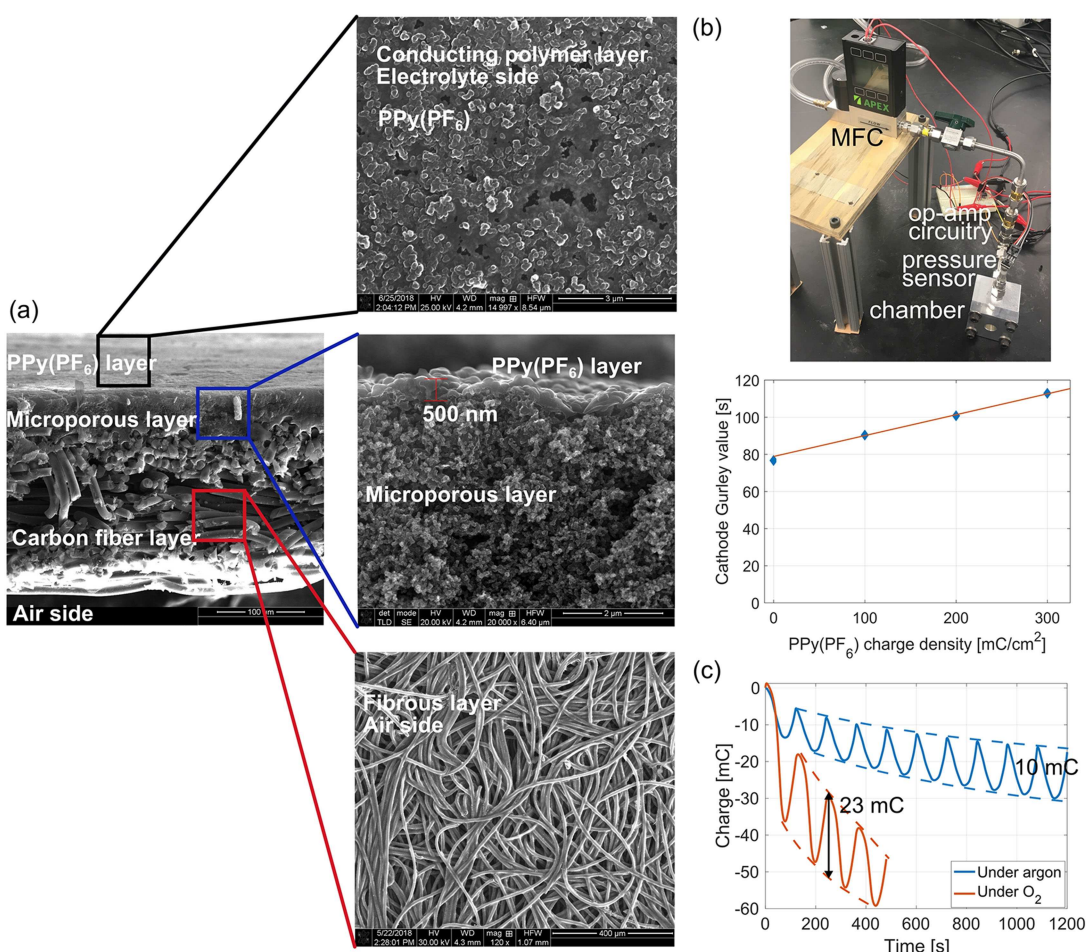


**Figure 3.** Structure and construction of FGC for  $\text{K}-\text{O}_2$  battery (a), characterization of oxygen permeability to estimate Gurley value (b), cyclic voltammetry of PPy( $\text{PF}_6^-$ ) in the presence of and absence of oxygen demonstrating the effect of ORR (scan rate  $20 \text{ mV s}^{-1}$ ) (c).

upon PPy(PF<sub>6</sub>) deposition by an average of 110 seconds per Ccm<sup>-2</sup> of PPy(PF<sub>6</sub>) deposited charge. Thus, the Gurley value varies between 85 and 120 seconds for deposited charge of 100 and 300 mCcm<sup>-2</sup>. The ability to control oxygen permeability through the cathode provides another degree of freedom via electropolymerization of PPy(PF<sub>6</sub>) in the design of FGC to regulate the battery performance. From the SEM, it is also observed that the three-dimensional morphology of micro-porous carbon layer makes it less likely for PPy(PF<sub>6</sub>) to completely span the pores between 100 mCcm<sup>-2</sup> and 300 mCcm<sup>-2</sup> than on a porous track-etched polycarbonate substrate.<sup>[23]</sup> In addition, the microporous carbon is highly hydrophobic (with one of the highest contact angles among commercial electrodes<sup>[11]</sup>) and prevents the aqueous polymerization solution from fully permeating into the pores. As a result, PPy(PF<sub>6</sub>) formed as a thin layer on top of the carbon as shown in the cross-section SEM in Figure 3(a) instead of throughout the thickness.

The PPy(PF<sub>6</sub>) layer is intended to support ORR in this FGC design besides regulation of oxygen transport across the cathode. ORR in PPy has been reported in earlier studies and follows the schematic shown in Figure 2(c). The redox sites in PPy(PF<sub>6</sub>) act as mediators for ORR and can only transfer an electron to oxygen in the reduced state.<sup>[25][26]</sup> The ORR is experimentally characterized by preparing PPy(PF<sub>6</sub>) on a porous stainless steel mesh following the description in SI. The SS mesh was soaked in the solution for 30 minutes before electropolymerization to promote uniform nucleation and deposition. After drying under vacuum, this cathode was assembled in a K–O<sub>2</sub> battery with 0.5 M KPF<sub>6</sub> in DME and characterized by CV before and after introducing O<sub>2</sub> in the cell. The cell was assembled in the same manner as described in SI Section 2.3. The CV is plotted as a charge versus time plot in Figure 3(c) and as the typical I–V curve in Figure S3. The reversible redox reactions PPy(PF<sub>6</sub>) undergoes in the cell in the presence of argon and oxygen are shown in Table 1.

**Table 1.** Reversible redox reactions of PPy(PF<sub>6</sub>) with and without ORR.

Under argon	Under oxygen
$\text{PPy}^+[\text{PF}_6^-] + e^- \leftrightarrow \text{PPy}^0 + \text{PF}_6^-$	$\text{PPy}^+[\text{PF}_6^-] + e^- \leftrightarrow \text{PPy}^0 + \text{PF}_6^-$ $\text{PPy}^0 + \text{O}_2 \rightarrow \text{PPy}^+ + \text{O}_2^-$ $\text{PPy}^+ + e^- \rightarrow \text{PPy}^0$ $\text{K}^+ + \text{O}_2^- \rightarrow \text{KO}_2$ $\text{PPy}^+ + [\text{PF}_6^-] \rightarrow \text{PPy}^+[\text{PF}_6^-]$

Under argon, the total charge exchanged per cycle approximately 10 mC. After oxygen was introduced, a reduction charge of  $\approx$ 23 mC of charge per cycle was observed, and this was attributed to ORR. Thus, the additional charge consumed to reduce oxygen is estimated to be  $\approx$ 13 mC. This study of ORR on PPy(PF<sub>6</sub>) demonstrates that PPy(PF<sub>6</sub>) meets the functional requirements for the proposed FGC. Thus, it is conclusively established that the PPy(PF<sub>6</sub>) in FGC does not cover the pores, forms on the surface of microporous carbon and supports ORR for enhanced consumption.

In order to evaluate the oxygen barrier properties of PPy(PF<sub>6</sub>) formed across the pores, oxygen permeability experiments were performed on PPy(PF<sub>6</sub>) formed across the pores of Celgard membranes. The results from these experiments summarized in SI indicate that PPy(PF<sub>6</sub>) forms a dense, non-porous membrane on the Celgard substrate, even at a low charge density of 100 mCcm<sup>-2</sup>. This result establishes that PPy(PF<sub>6</sub>) completely blocks transmembrane oxygen transport and functions as an oxygen barrier membrane when deposited on Celgard.

### 3. K–O<sub>2</sub> Battery Characterization

K–O<sub>2</sub> batteries with different types of cathode configurations shown in Table 2 were assembled following the steps outlined in SI. The Swagelok cell used for battery construction and cell materials are shown in Figure 4(a), and charge/discharge cycles for each battery are shown in Figure 4(b–f). The batteries were tested by galvanostatic charge/discharge cycles (3-hour charge and 3-hour discharge at 100  $\mu$ A) with cut-off voltages of 3.0 and 2.0 V respectively. These experimental protocols were chosen to be comparable with existing work.<sup>[6,8]</sup>

The baseline battery became unstable during the fourth cycle and did not charge or discharge thereafter. Visual inspection of the anode reveals a thin pale-yellow layer of deposits similar in appearance to the observations made by Wu and coworkers<sup>[4,5]</sup> and is attributed to the side reactions at the anode resulting from oxygen crossover. The side products passivate the anode surface resulting in a rapid loss of cyclability of the baseline battery. The oxygen barrier cathode battery had a fast voltage decay in the first cycle, reaching the cut-off potential in about 20 minutes. It did not charge or discharge on subsequent cycles, but no KO<sub>2</sub> was observed on the anode upon disassembly. The most likely failure mode for

**Table 2.** K–O<sub>2</sub> batteries assembled to investigate the functionality of FGC.

Configuration name	Anode	Membrane separator	Electrolyte	Cathode
Baseline battery	K metal	Glass fiber	DME + KPF <sub>6</sub>	Electrospun fibrous carbon mat + Microporous carbon
Oxygen barrier cathode battery	K metal	Glass fiber	DME + KPF <sub>6</sub>	Electrospun fibrous carbon mat + Microporous carbon + Porous polypropylene (Celgard) + PPy(PF <sub>6</sub> )
FGC100	K metal	Glass fiber	DME + KPF <sub>6</sub>	Electrospun fibrous carbon mat + Microporous carbon + 100 mCcm <sup>-2</sup> PPy(PF <sub>6</sub> )
FGC200	K metal	Glass fiber	DME + KPF <sub>6</sub>	Electrospun fibrous carbon mat + Microporous carbon + 200 mCcm <sup>-2</sup> PPy(PF <sub>6</sub> )
FGC300	K metal	Glass fiber	DME + KPF <sub>6</sub>	Electrospun fibrous carbon mat + Microporous carbon + 300 mCcm <sup>-2</sup> PPy(PF <sub>6</sub> )

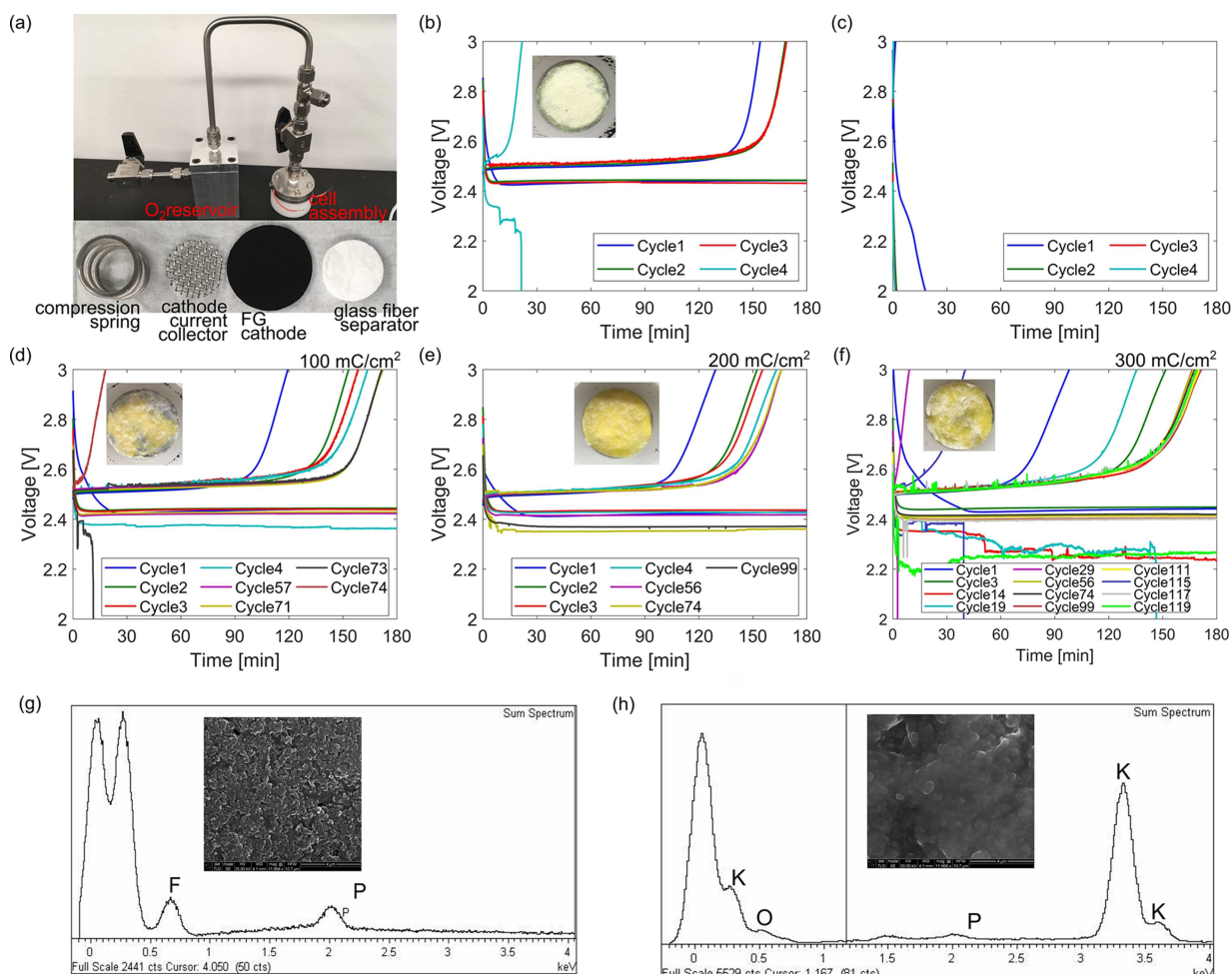


**Figure 4.** Custom Swagelok K–O<sub>2</sub> battery and materials used for assembly (a), cycling results for the baseline battery (b), oxygen barrier cathode battery (c), functionally graded cathode (FGC) batteries (d–f) [(d) FGC100, (e) FGC200, (f) FGC300], EDX spectra pristine PPy(PF<sub>6</sub>) layer of FG cathode ( $200 \text{ mC cm}^{-2}$ ) [SEM image inset] (g), and EDX spectra of PPy(PF<sub>6</sub>) layer of FGC ( $200 \text{ mC cm}^{-2}$ ) after battery cycling [SEM image inset] (h).

this cathode configuration was the low potassium ion conductivity of the dense PPy(PF<sub>6</sub>) membrane. It is known from Hery and Sundaresan that pore-spanning anion doped PPy membranes can transport cations in its reduced state.<sup>[23]</sup> In this oxygen barrier cathode, PPy(PF<sub>6</sub>) becomes impervious to K<sup>+</sup> ions and prevents the battery from discharging/charging as observed in Figure 4(c). Therefore, low K<sup>+</sup> conductivity of PPy(PF<sub>6</sub>) as an oxygen barrier cathode precludes its use in K–O<sub>2</sub> battery despite low oxygen crossover.

The K–O<sub>2</sub> battery with FGC cycled longer and performed with a consistent charge/discharge cycles as shown in Figure 4(d–e). The FGC100 battery cycled up to 72 cycles before it began experiencing significant instability in the charge/discharge profiles (Figure 4(d)). The FGC200 battery had a longer cycle-life (and about 575 hours lifetime) and still discharged fully at the 100<sup>th</sup> cycle (Figure 4(e)). The FGC300 battery cycled up to 120 cycles and it is observed that charging/discharging were not always stable (Figure 4(f)). Instabilities were observed in some of the charge/discharge cycles in FGC200 and FGC300 batteries, but the battery resumed normal operation shortly thereafter.

The SEM image of the PPy(PF<sub>6</sub>) layer of an as prepared FGC is shown inset in Figure 4(g). As intended, the PPy partially covers the pores of microporous carbon, and the average pore size has decreased compared to plain microporous carbon. The EDX spectra in Figure 4(g) shows P and F peaks which confirm that PPy has been doped with hexafluorophosphate during polymerization. At the end of cycling the membrane in battery charging/discharging tests, the cathodes are rinsed in DME, and a post-mortem SEM and EDX of the PPy side is performed. The results shown inset in Figure 4(h) shows that the surface is covered with the discharge product and the EDX data in Figure 4(h) shows K and O peaks compared to the pristine cathode. This indicates that KO<sub>2</sub> is formed at the cathode/separator interface and not just at the air-facing side of the cathode. The microporous carbon and PPy(PF<sub>6</sub>) impedes flow of oxygen and the increased ORR activity at the PPy-layer further limits the transport of oxygen to the anode. The discharge product on the PPy surface is anticipated to be KO<sub>2</sub>, but it does not have the typical crystalline morphology that is characteristic of KO<sub>2</sub> on carbon-based cathodes. The EDX analysis of Figure 4(h) indicates that the atomic percentages of K and O to

be 33 and 65% respectively, suggesting that  $\text{KO}_2$  is the discharge product. It should also be noted that recent reports indicate the formation of  $\text{K}_2\text{O}_2$  at low potentials ( $\sim 2.25 \text{ V}$  vs  $\text{K}/\text{K}^+$ ) on gold electrodes in acetonitrile.<sup>[27]</sup> In the characterization studies reported in this paper, the discharge potentials largely remain outside of this window (in charge/discharge data in Figure 4) and therefore  $\text{KO}_2$  is the expected discharge product. Previous studies have shown that the average crystal size of  $\text{KO}_2$  decreases with increasing discharge rate.<sup>[28]</sup> During discharge, some percentage of the current will go to PPy( $\text{PF}_6$ ) and the remaining will go to carbon depending on the relative surface areas and activities for ORR. The majority of the FGC surface area is carbon, but the majority of the current initially goes to PPy( $\text{PF}_6$ ) due to the lower energy barrier for ORR. The ORR exchange current density of PPy( $\text{PF}_6$ ) is estimated to be nearly two orders of magnitude higher than that of carbon based on linear cathodic sweeps of each cathode (found in SI). Therefore, it is likely that the net discharge rate from PPy( $\text{PF}_6$ ) layer is very high and the  $\text{KO}_2$  crystal size is very small.

The overpotential and coulombic efficiency of FGC batteries are compared with the baseline battery during cycling experiments and shown in Figure 5. The overpotential for the baseline battery starts around 100 mV with a coulombic efficiency of 55%. The overpotential increases very rapidly to about 800 mV by the 4<sup>th</sup> cycle and stops cycling by the 5<sup>th</sup> cycle. This irreversible increase in overpotential and drop in coulombic efficiency is attributed to the passivation of anode and hence this battery is considered to have reached its end of life.

The FGC batteries (FGC100, FGC200 and FGC300) starts with a low overpotential of  $\sim 100 \text{ mV}$  at the start of cycling experiments. The coulombic efficiency starts at about 55–70% and rapidly increases to 96% and remains at around 95% until failure. The overpotential for FGC200 and FGC300 batteries begins to fluctuate and stabilizes within 10–15 cycles of continuous cycling. The overpotential for FGC100 remains more stable than FGC200 and FGC300 until failure by around the 70<sup>th</sup> cycle. The rapid increase in overpotential to 1.4 V occurs with loss of cyclability in FGC100 battery. The fluctuation in FGC200 and FGC300 overpotential between 15<sup>th</sup> and 25<sup>th</sup> cycle is transient, and it is observed that these batteries continue cycling for  $>100$  cycles. It is noted that the coulombic efficiency is greater than 80% even with the fluctuations

observed in overpotential during the charge/discharge cycle. The transient increase in overpotential for FGC200 and FGC300 battery are attributed to the formation of discharge products that prevent the diffusion of  $\text{K}^+$  into the cathode. The likelihood of clogging increases as PPy( $\text{PF}_6$ ) charge density increases. This explains why the thickest and least porous PPy( $\text{PF}_6$ ) layer (Figure 4(f)) experiences the most instability. Upon subsequent charging, it is proposed that the discharge products are converted back to  $\text{K}^+$  and  $\text{O}_2$  and hence the battery returns to normal cycling during subsequent discharge cycles. It is observed that instabilities return to FGC200 and FGC300 by around 70<sup>th</sup> cycle and 120<sup>th</sup> cycle respectively and the coulombic efficiency drops to between 5% and 1% with loss in cyclability. The irreversible increase in overpotential and drop in coulombic efficiency is attributed to the formation of passivation layer in the anode as observed from the post-mortem analysis. Thus, it is proposed that a combination of rapid fluctuations in overpotential and drop in coulombic efficiency can be simultaneously used for evaluating the health of  $\text{K}-\text{O}_2$  battery as observed from these cycling studies.

The high coulombic efficiency and low overpotential of  $\text{K}-\text{O}_2$  battery with functionally graded cathodes offer an alternative to designing  $\text{K}-\text{O}_2$  battery with a cycle-life of greater than 100. The cost added to the  $\text{K}-\text{O}_2$  battery due to the inclusion of PPy( $\text{PF}_6$ ) is  $\$0.84 \text{ kWh}^{-1}/100 \text{ mC cm}^{-2}$  as shown in Figure 5(c) and detailed calculations are presented in SI. Thus, for a material cost of about  $\$44 \text{ kWh}^{-1}$  the FGC  $\text{K}-\text{O}_2$  battery offers an economically viable pathway to produce  $\text{K}-\text{O}_2$  battery with cyclability ( $> 100$  cycles) over alternatives.<sup>[8]</sup>

The mechanism by which FGC limits oxygen crossover is presented by modeling the oxygen concentration in the cathode during discharge using Equations 1–3. The cathode is modeled as a combination of cylindrical particles for the carbon fiber layer and spherical particles for the PPy and microporous layers (Figure 6(a)). The parameters required for this model obtained using SEM images, CV data, and reported values is listed in Table 3. Necessary calculations to obtain derived values from reported values are presented in SI.

It is assumed that the porosity of FGC does not vary significantly during discharge and therefore the effect of structural changes due to the accumulation of discharge products is neglected. This assumption is based on previous work that has shown the full capacity of carbon-fiber cathode

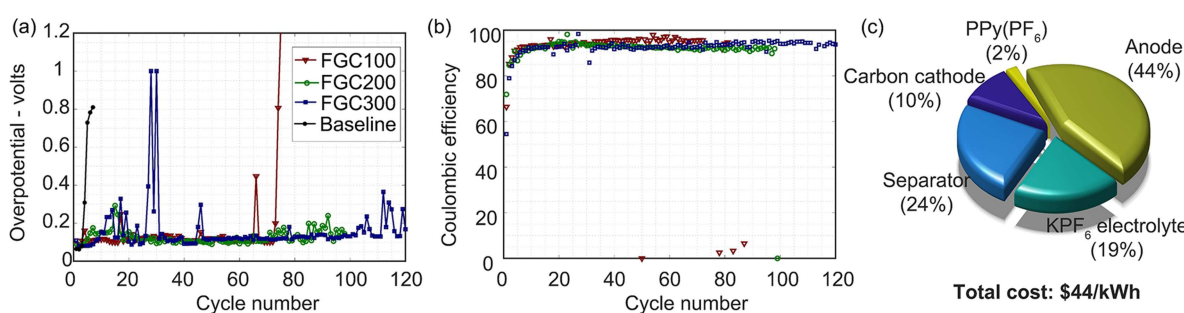


**Figure 5.** Comparison of overpotentials (a) and coulombic efficiency (b) for  $\text{K}-\text{O}_2$  battery with functionally graded cathodes for different areal charge densities of PPy( $\text{PF}_6$ ) from cycling data, and cost breakdown for  $\text{K}-\text{O}_2$  battery with FGC cathode (c).

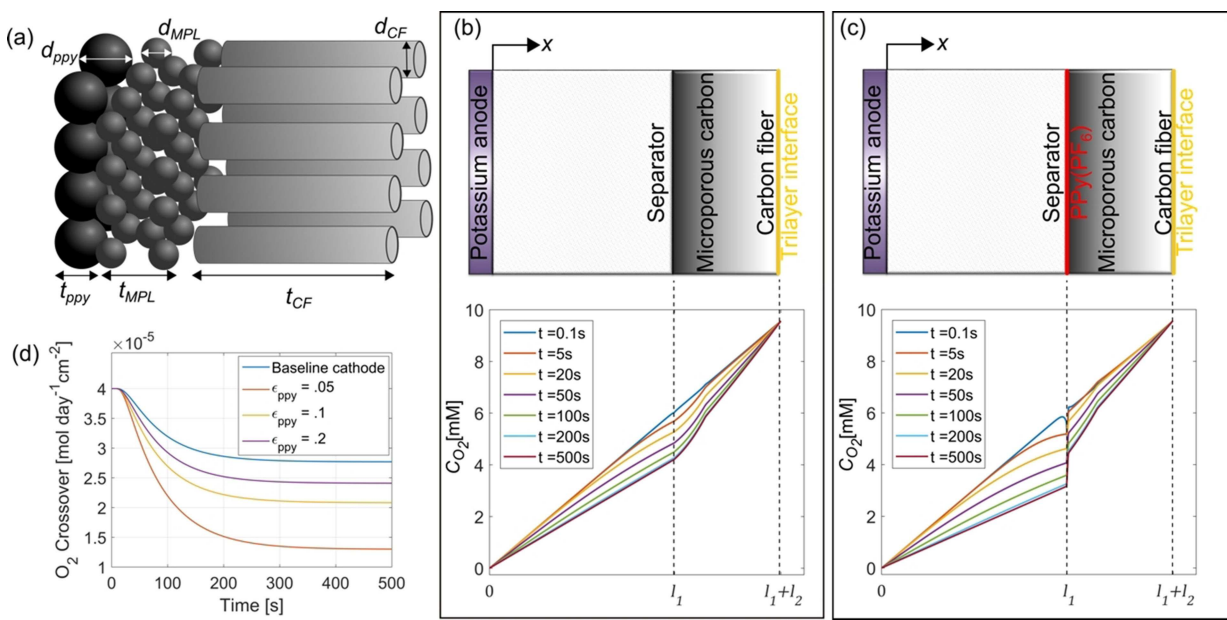


**Figure 6.** Modeling of oxygen concentration gradient in K–O<sub>2</sub> battery. Cathode particle model with PPy(PF<sub>6</sub>) and microporous carbon modeled as spherical particles and carbon fiber layer modeled as cylindrical particle (a), baseline cathode oxygen gradient upon start of discharge until steady state (b), FG cathode oxygen gradient assuming a PPy(PF<sub>6</sub>) porosity of 10% (c) and oxygen crossover rate versus time for baseline cathode and FG cathode with different PPy(PF<sub>6</sub>) porosities (d).

**Table 3.** Simulation parameters for modeling oxygen concentration between the electrodes in a K–O<sub>2</sub> battery with functionally graded cathode.

General Parameters	Description	Value	Source
$D_{\text{O}_2}$	oxygen diffusion coefficient in DME	$1.22 \times 10^{-5} \text{ cm}^2 \text{s}^{-1}$	[29]
$C_{\text{O}_2}^{\text{ef}}$	O <sub>2</sub> solubility limit in DME	9.6 mM	[30]
$l_1$	separator thickness	400 μm	
$l_2$	cathode thickness	230 μm	Datasheet
$t_{\text{ppy}}$	PPy(PF <sub>6</sub> ) layer thickness	0.6 μm	SEM
$t_{\text{MPL}}$	microporous layer thickness	50 μm	SEM
$t_{\text{CF}}$	carbon fiber layer thickness	170 μm	SEM
$\beta$	Tafel equation symmetry factor	0.5	
$\varepsilon_s$	compressed separator porosity	0.5	
$i_{\text{geom}}$	discharge current density	0.079 mA cm <sup>-2</sup>	
Fibrous Carbon Parameters			
$\varepsilon_{\text{CF}}$	carbon fiber layer porosity	0.5	[11]
$d_{\text{CF}}$	carbon fiber diameter	10 μm	SEM
$i_{\text{o},B}$	ORR exchange current density	$5.84 \times 10^{-8} \text{ A cm}^{-2}$	
$A_s$	specific surface area	$4(1-\varepsilon_{\text{CF}})/d_{\text{CF}} \text{ m}^2 \text{ m}^{-3}$	[14]
Microporous Layer Parameters			
$\varepsilon_{\text{MPL}}$	microporous layer porosity	0.4	
$d_{\text{MPL}}$	microporous layer particle diameter	0.1 μm	SEM
$i_{\text{o},B}$	ORR exchange current density	$5.84 \times 10^{-8} \text{ A cm}^{-2}$	
$A_s$	specific surface area	$6(1-\varepsilon_{\text{MPL}})/d_{\text{MPL}} \text{ m}^2 \text{ m}^{-3}$	[14]
PPy(PF <sub>6</sub> ) Layer Parameters			
$\varepsilon_{\text{ppy}}$	PPy(PF <sub>6</sub> ) layer porosity	0.05–0.2	
$d_{\text{ppy}}$	PPy(PF <sub>6</sub> ) layer particle diameter	0.15 μm	SEM
$i_{\text{o},\text{ppy}}$	ORR exchange current density	$3.5 \times 10^{-6}$ – $4.2 \times 10^{-6} \text{ A cm}^{-2}$	
$A_s$	specific surface area	$6(1-\varepsilon_{\text{ppy}})/d_{\text{ppy}} \text{ m}^2 \text{ m}^{-3}$	[14]

in K–O<sub>2</sub> battery is >10 times larger than the charge consumed during one cycle here.<sup>[28]</sup> The boundary conditions at the anode surface and air side are as follows:

$$C_{O_2}(t, 0) = 0 \quad (4)$$

$$C_{O_2}(t, l_1 + l_2) = C_{O_2}^{ref} \quad (5)$$

where  $C_{O_2}^{ref}$  is the oxygen solubility in the electrolyte. The boundary condition at the anode assumes that any oxygen is immediately consumed upon reaching the anode surface. It is difficult to determine the accuracy of this assumption, but it is a worst-case scenario for maximum O<sub>2</sub> crossover. The initial condition assumes a linear decrease in oxygen concentration from the air side to the anode before start of discharge:

$$C_{O_2}(0, x) = \frac{C_{O_2}^{ref}}{l_1 + l_2} x \quad (6)$$

The model is solved using a finite difference method for both the baseline battery (Figure 6(b)) and FGC battery (Figure 6(c)) until a steady state is reached. This model assumes a range of PPy(PF<sub>6</sub>) porosities for simulation based on SEM images. It is assumed PPy(PF<sub>6</sub>) porosity is 20% (most porous PPy(PF<sub>6</sub>)-FGC100), 10% (FGC200) and 5% (least porous PPy(PF<sub>6</sub>)-FGC300) in the functionally graded cathodes.

The results from solving the equations indicate that the oxygen crossover becomes asymptotic to steady state flux for both the baseline battery and FGC at around 200 seconds as shown in Figure 6(d). The steady state crossover rate for the cathode in baseline battery is  $2.77 \times 10^{-5}$  mol day<sup>-1</sup> cm<sup>-2</sup> and the presence of PPy(PF<sub>6</sub>) layer in FGC causes a decrease in oxygen flux of 13% for FGC100 battery, 25% for FGC200 battery and 53% for FGC300 battery.

The oxygen concentration for the FGC near the cathode/separator interface in Figure 6(c-bottom tile) decreases sharply compared to that for the baseline cathode (Figure 6(b-bottom tile)). It is observed from comparing the bottom tiles in Figure 6(b) and Figure 6(c) that oxygen concentration in cathode with PPy(PF<sub>6</sub>) is greater than in the baseline battery. The results from characterization of ORR in PPy(PF<sub>6</sub>) layer in FGC indicated at least two orders increase in ORR exchange current density over carbon. From these results, it is proposed that the increase in cyclability of K–O<sub>2</sub> battery is due to a combination of the following occurring at the cathode – (i) higher oxygen concentration, (ii) higher ORR exchange current density and (iii) smaller size of discharge products (KO<sub>2</sub>). In the case of FGC100 and FGC200 batteries, the stability of the recorded overpotential supports this explanation. It should be noted that in FGC300 battery, the fluctuating overpotential indicates irreversible reactions that lead to higher internal impedance and ultimate failure to charge/discharge.

## 4. Conclusions

A porous functionally graded cathode with PPy(PF<sub>6</sub>) is demonstrated in this article to increase the useful cycle-life of K–O<sub>2</sub> battery. The polypyrrole layer added to the porous cathode at the electrolyte-separator interface is shown to serve two functions – (i) block the diffusion of gas phase reactants (during discharging) and products (during charging) into the electrolyte and (ii) enhance ORR and consume molecular oxygen at the cathode. The polypyrrole layer added to the cathode is observed to have two orders of increased ORR during discharge reactions and hence decreases the resident time for molecular oxygen at the cathode. This minimizes the probability for the diffusion of molecular oxygen to the anode following the analysis in oxygen transport model. It should be noted that this charge/discharge currents during cycling of the K–O<sub>2</sub> battery is approximately twice as much as comparable studies. It is shown that materials cost of a K–O<sub>2</sub> battery with a porous carbon cathode is about \$43 kWh<sup>-1</sup> and that of a K–O<sub>2</sub> battery with functionally graded cathode increases to \$44 kWh<sup>-1</sup>. At this cost, cycle-life of greater than 100 cycles (or 500+ hours at a capacity of 238 μAh cm<sup>-2</sup>), this mechanistic design for the cathode is presented as a practically feasible alternative over other approaches for the K–O<sub>2</sub> battery.

## Acknowledgements

This work was funded by the National Science Foundation under an award (#1512405) from Energy for Sustainability program in the Division of Chemical, Biological and Engineering Transport Systems. The authors would like to thank Prof. Yiyang Wu and Neng Xiao (Department of Chemistry and Biochemistry) and Prof. Noriko Katsumata (Department of Mechanical and Aerospace Engineering) at The Ohio State University for discussions and feedback towards this manuscript.

## Conflict of Interest

The authors declare no conflict of interest.

**Keywords:** potassium-air batteries • functionally graded cathode • oxygen reduction reaction • oxygen crossover • electrode design

- [1] J. S. Lee, S. T. Kim, R. Cao, N. S. Choi, M. Liu, K. T. Lee, J. Cho, *Adv. Energy Mater.* 2011, 1, 34.
- [2] J. Lu, L. Li, J. B. Park, Y. K. Sun, F. Wu, K. Amine, *Chem. Rev.* 2014, 114, 5611.
- [3] L. Grande, E. Paillard, J. Hassoun, J. B. Park, Y. J. Lee, Y. K. Sun, S. Passerini, B. Scrosati, *Adv. Mater.* 2015, 27, 784.
- [4] X. D. Ren, Y. Y. Wu, *J. Am. Chem. Soc.* 2013, 135, 2923.
- [5] X. Ren, K. Lau, M. Yu, X. Bi, E. Kreidler, L. Curtiss, Y. Wu, *ACS Appl. Mater. Interfaces* 2014, 6, 19299.
- [6] X. Ren, M. He, N. Xiao, W. McCulloch, Y. Wu, *Adv. Energy Mater.* 2017, 7.
- [7] W. D. McCulloch, N. Xiao, G. Gourdin, Y. Y. Wu, *Chem. Eur. J.* 2018, 24, 17627.

- [8] N. Xiao, G. Gourdin, Y. Wu, *Angew. Chem. Int. Ed.* **2018**, *57*, 10864.  
[9] D. L. Wood, J. L. Li, C. Daniel, *J. Power Sources* **2015**, *275*, 234.  
[10] D. Myung, J. Hwang, J. Hong, H. Lee, B. Kim, J. Lee, J. Son, *J. Electrochem. Soc.* **2011**, *158*, B1000.  
[11] A. El-Kharouf, T. J. Mason, D. J. L. Brett, B. G. Pollet, *J. Power Sources* **2012**, *218*, 393.  
[12] P. Tan, W. Shyy, L. An, Z. H. Wei, T. S. Zhao, *Electrochem. Commun.* **2014**, *46*, 111.  
[13] S. S. Sandhu, J. P. Fellner, G. W. Brutchen, *J. Power Sources* **2007**, *164*, 365.  
[14] X. Li, J. Huang, A. Faghri, *J. Power Sources* **2016**, *332*, 420.  
[15] P. Andrei, J. Zheng, M. Hendrickson, E. Plichta, *J. Electrochem. Soc.* **2010**, *157*, A1287.  
[16] R. V. Parthasarathy, V. P. Menon, C. R. Martin, *Chem. Mater.* **1997**, *9*, 560.  
[17] D. V. Andreeva, Z. Pientka, L. Brozova, M. Bleha, G. A. Polotskaya, G. K. Elyashevich, *Thin Solid Films* **2002**, *406*, 54.  
[18] N. Togasaki, R. Shibamura, T. Naruse, T. Momma, T. Osaka, *APL Mater.* **2018**, *6*.  
[19] T. Yuan, J. F. Ruan, W. M. Zhang, Z. P. Tan, J. H. Yang, Z. F. Ma, S. Y. Zheng, *ACS Appl. Mater. Interfaces* **2016**, *8*, 35114.  
[20] S. Demoustier-Champagne, P. Y. Stavaux, *Chem. Mater.* **1999**, *11*, 829.  
[21] Y. M. Cui, Z. Y. Wen, X. Liang, Y. Lu, J. Jin, M. F. Wu, X. W. Wu, *Energy Environ. Sci.* **2012**, *5*, 7893.  
[22] K. Kim, W. G. Lee, *New J. Chem.* **2017**, *41*, 1321.  
[23] T. Hery, V. B. Sundaresan, *Energy Environ. Sci.* **2016**, *9*, 2555.  
[24] R. Northcutt, V. B. Sundaresan, *Smart Mater. Struct.* **2012**, *21*.  
[25] E. Nasibulin, W. Xu, M. H. Engelhard, X. H. S. Li, M. Gu, D. H. Hu, J. G. Zhang, *Electrochem. Commun.* **2013**, *29*, 63.  
[26] V. G. Khomenko, V. Z. Barsukov, A. S. Katashinskii, *Electrochim. Acta* **2005**, *50*, 1675.  
[27] Y. Chen, Z. Jovanov, X. Gao, J. Liu, C. Holc, L. Johnson, P. Bruce, *J. Electroanal. Chem.* **2018**, *819*, 542.  
[28] N. Xiao, X. D. Ren, M. F. He, W. D. McCulloch, Y. Y. Wu, *ACS Appl. Mater. Interfaces* **2017**, *9*, 4301.  
[29] C. Laoire, S. Mukerjee, K. Abraham, E. Plichta, M. Hendrickson, *J. Phys. Chem. C* **2010**, *114*, 9178.  
[30] J. Read, K. Mutolo, M. Ervin, W. Behl, J. Wolfenstine, A. Driedger, D. Foster, *J. Electrochem. Soc.* **2003**, *150*, A1351.

Manuscript received: February 15, 2019

Revised manuscript received: March 20, 2019

Accepted manuscript online: April 5, 2019

Version of record online: May 10, 2019